Taylor & Francis
Taylor & Francis Group

A filter-based post-processing technique for improving homogeneity of pixel-wise classification data

Tung-Ching Su

European Journal of Remote Sensing
An official journal of the Italian Society of Remote Sensing

www.aitjournal.com

A filter-based post-processing technique for improving homogeneity of pixel-wise classification data

Tung-Ching Su*

Department of Civil Engineering and Engineering Management,
National Quemoy University, 1 Da Xue Rd., 89250 Kinmen, Taiwan
*Corresponding author, e-mail address: spcyj@nqu.edu.tw

Abstract

Many studies have presented various classification techniques for improving the accuracy of image classification, but heterogeneous classification results, like salt-and-pepper still appear in thematic maps. In this paper, a filter-based post-classification technique, likelihood class filter (LCF), is presented to not only remove heterogeneous classes but also to improve the accuracy of image classification. This paper demonstrates that the classification accuracy can be effectively improved by LCF, which offers the resulting thematic maps of Salinas-A scene, Indian Pines test site and Pavia University scene the optimal overall accuracy (the highest homogeneity index) of 99.81% (0.9716), 92.41% (0.8936) and 92.35% (0.8985), respectively.

Keywords: Image classification, post-processing, likelihood class filter (LCF), homogeneity.

Introduction

The high-dimensional feature space of remote sensing data poses challenges to image processing and classification techniques due to the large number of spectral channels and the relatively small number of label samples [Zhang and Huang, 2010]. Without considering the relationship between spatial and spectral properties, pixel-wise image classification techniques would probably cause salt-and-pepper classification results [Yang, 2007; Huang and Zhang, 2008; Du et al., 2012; Velasco-Forero and Angulo, 2013]. To tackle the above problems, spectral mixture analyses transforming radiance data into fractions of a few dominant endmember spectra corresponding to scene components and feature extraction approaches have been presented [Tarabalka et al., 2010; Zhang and Huang, 2010; Kumar et al., 2010; Villa et al., 2013; Huang and Huang, 2014; Sun et al., 2014].

Reducing the dimensionality of remote sensing data without the loss of information before classification is an important and urgent issue [Huang and Huang, 2014; Sun et al., 2014]. In the past decade, feature extraction has usually focused on imagery classification [Chen and Ho, 2008; Zhang and Huang, 2010; Mura et al., 2011; Licciardi et al., 2012; Velasco-Forero and Angulo, 2013; Marpu et al., 2013; Huang and Huang, 2014]. The results

demonstrate that their proposed feature extraction methods are accurate when limited and sufficient samples are used. In pixel-wise classification, support vector machine (SVM), one of the kernel-based methods, has recently shown good classification results because of its robust capacity under a limited number of available training samples, and presents better performances compared to other supervised techniques [Gualtieri et al., 1999; Yang and Su, 2008; Plaza et al., 2009; Tarabalka et al., 2010; Samadzadegan et al., 2012; Su and Du, 2014]. Several spectral-spatial classification techniques based on SVM have been proposed, and the classification accuracies of remote sensing data have been improved [Plaza et al., 2009; Tarabalka et al., 2010; Zhang and Huang, 2010; Mura et al., 2011; Velasco-Forero and Angulo, 2013; Marpu et al., 2013; Akbari et al., 2014; He and Li, 2015]. However, these spectral-spatial classification techniques usually involve complicated mathematical transformations. Furthermore, heterogeneous classes like salt-and-pepper noise may still occur in the thematic maps of spectral-spatial classification.

In order to eliminate the salt-and-pepper noise phenomenon, this paper focuses on post-processing techniques for pixel-wise classification data, rather than on novel feature extraction or spectral-spatial classification, for homogeneity improvement. Recently, several post-classification techniques have been proposed to improve the accuracy of image classification or segmentation. Ouma and Tateishi [2008] indicated that the traditional pixel-wise statistic and monoscale based classification approaches do not lead to satisfactory results due to the more heterogeneous spectral-radiometric characteristics within urban land-use/cover units in very high spatial resolution imagery. They applied a 3×3 post-classification "smoothing filter" to eliminate the "salt-and-pepper" appearances of the classified image. Tu et al. [2014] presented a novel combined post-filtering method, which uses a weighted median filter, a bilateral filter and a fast median filter, to post-smooth the detected edges and occlusions, and the other flat regions of the flow field, respectively. García-Gutiérrez et al. [2015] showed a novel contextual classifier based on SVM and Evolutionary Majority Voting (SVM-EMV) to develop thematic maps from LiDAR and imagery data. The voting system selected the most common label among the neighbours, taking into account that each neighbour vote was weighted according to the distance to the pixel to be reclassified.

In this research, due to its good performance in dimensionality reduction [Zhang and Huang, 2010], Minimum Noise Fraction (MNF), one of the feature extraction methods, was used to first extract n eigenimages, which denote robustly distinct features, from remote sensing data. Then, SVM was introduced to image classification based on the extracted eigenimages. After the pixel-wise classification by SVM, the obtained thematic maps would suffer from the salt-and-pepper noise phenomenon unless the relationship between spatial and spectral properties was insignificant. In order to eliminate the salt-and-pepper effect, this study proposed a post-classification technique which called likelihood class filter (LCF), developed based on the principle of low-pass filtering. The operation of LCF is similar to that of traditional low-pass filters, but instead of high-frequency spectral information, heterogeneous class is filtered. LCF is based on a thematic map, removing heterogeneous classes from the map. Simultaneously, classification accuracy is improved by transforming heterogeneous classes into homogeneous ones. In addition, the post classification tools of ENVI, including "Majority Analysis", "Sieve Classes" and "Clumping Classes", are also similar in function to LCF. In "Majority Analysis", the operation needs a given centre pixel

weight to perform majority analysis, but the centre pixel weight in LCF is automatically determined by one of the 8 neighbourhood classes which has the most pixels. In "Sieve Classes", the operation needs a given group min threshold to perform sieving analysis considering 4 or 8 neighbours, but LCF, where the 8 neighbours are also considered, can automatically decide whether the class of the central pixel in the kernel needs to be changed or not. In "Clumping Classes", the analysis is implemented based on morphological operations. Thus, LCF would appear to be an integration of "Majority Analysis" and "Sieve Classes".

Methodology

The process of feature extraction by MNF through pixel-wise classification by SVM can be found in many studies, so the contents of MNF and SVM are briefly described as follows. This section focuses on the LCF algorithm and the evaluation method of homogeneity improvement.

Feature extraction with MNF

MNF is an improved version of principal component analysis, and is able to determine the inherent dimensionality of feature space, to segregate noise in the data, and to reduce the computational cost for subsequent processing. The following is an additive noise model:

$$Z(x) = S(x) + N(x) \quad [1]$$

where $Z(x)$ is the original signal, and $S(x)$ and $N(x)$ denote the uncorrelated signal and noise components of $Z(x)$, respectively. The covariance matrices can be related by:

$$Cov(Z(x)) = \Sigma_S + \Sigma_N \quad [2]$$

where Σ_S and Σ_N represent the signal and noise covariance matrices, respectively. The noise portion for band m is defined as:

$$Var(N_m(x)) / Var(Z_m(x)) \quad [3]$$

where Var($\cdot$) means the variance. MNF transformation creates new uncorrelated images based on a linear transformation of the original data set, $Y=A^{\mathsf{T}}Z$, where the transformation matrix A is calculated by solving the eigenvalue equation:

$$A\Sigma_N \Sigma_S^{-1} = \Lambda A \quad [4]$$

where $\Lambda=(\lambda_1, \lambda_2, \ldots, \lambda_n)$ is a diagonal matrix of the eigenvalues, i.e. $\lambda_1, \lambda_2, \ldots, \lambda_n$. MNF transformation arranges the feature bands according to the decrease of noise portion, and extracts the subspace of an image by analysing the proportion of the noise variance described by the first several MNF bands. Consequently, the noise portion, $N(x)$, can be

separated from the data, $Z(x)$, while only the coherent eigenimages are used to improve the performance of the spectral analysis.

Classification with SVM

Originally, SVM was designed to handle binary classes. For real-world decision surfaces, including the problem of hyperspectral image classification, several kernels are used to nonlinearly map the input data X_i, from a sample space into a high-dimensional feature space where the implementation of linear separation becomes much easier [Du et al., 2010; Tarabalka et al., 2010; Zhang and Huang, 2010]. In the nonlinear case, kernel functions, such as polynomial or RBF, must be used for the data transformation to establish a hyperplane for the nonlinear training pattern as:

$$w_0 \cdot \varphi(x) + b_0 = \left(\sum_{i=1}^{k} \alpha_i y_i \varphi(x_i) \right) \cdot \varphi(x) + b_0 \quad [5]$$

where w_0 and b_0 can determine the optimal separating hyperplane and are written as:

$$w_0 = \sum_{i=1}^{k} \alpha_i y_i x_i \quad [6]$$

$$b_0 = y_i - w_0 \cdot x_i \quad [7]$$

where x_i belongs to the support vectors $y_i \in \{-1,1\}$, and $\alpha_i \geq 0$ are the Lagrange multipliers. In Equation [5], $\varphi(x_i) \cdot \varphi(x)$ denotes the kernel function $K(x_i, x)$. The decision rule for the nonlinear training patterns can be established as:

$$f(x) = \textbf{\textit{sign}} \left(\sum_{i=1}^{k} \alpha_i y_i K(x_i, x) + b_0 \right) \quad [8]$$

Post-processing by likelihood class filter (LCF)

In this paper likelihood class filter is designed as a kernel with $M \times M$ elements. Generally, M must be an odd number above or equal to 3 so that the kernel has only a central element to be filtered [Yang et al., 1995]. A kernel with 3×3 elements for example, LCF based on the 8-neighborhood classes assigns a likelihood class for the central element. Note that the pixels on the edge of the thematic map are not taken into account by the LCF algorithm because the 3×3 kernel cannot be full of elements. Adopting a large kernel could lead to a better LCF result, but sometimes several meaningful classes with small spatial structures might be removed, thereby decreasing overall accuracy (OA). Moreover, a longer computation time would be needed. The filter of LCF algorithm was given as 3×3 kernel in this paper, so there are only two conditions as follows considered for likelihood class assignment of

the central element of the filter. The illustration of the likelihood class assignments using a 3×3 kernel is shown in Figure 1.

- One and only neighbourhood class consisting of absolutely major elements (condition I): In a 3×3 kernel, one and only neighbourhood class consisting of p or more elements has the absolute priority of being the likelihood class. In this research, p=5, 6, 7 and 8 were tested. While p is given as 5, the LCF algorithm can lead to the greatest thematic map transformation because 5 or more elements have included 6, 7 or 8 elements.
- Neighbourhood class consisting of relatively major elements (condition II): This condition means that the likelihood class is determined by a comparison of the number of elements among the neighbouring classes. The neighbouring class consisting of the largest number of elements is selected as the likelihood class. If there are neighbouring classes with an equal number of elements, the original class at the central element is retained. Thus, condition II also has included condition I and leads to a greater thematic map transformation than condition I. However, it is noticed that condition II may result in an over transformation to deteriorate classification accuracy.

The LCF algorithm is encoded in Matlab and described as follows:

Step 1: Import classification thematic map ($\mathbf{I}_{m \times n}$); the subscripts m and n mean the number of pixels in the row and column directions, respectively;

Step 2: List the neighbouring classes ($\mathbf{NC}_l(e)$) for the pixels, but excluding those on the edge of $\mathbf{I}$; the subscript l expresses the number of $\mathbf{NC}$s; e denotes the number of elements belonging to the lth $\mathbf{NC}$;

Step 3: Based on one of the two conditions of the likelihood class assignment, assign the likelihood class for the pixels, but excluding those on the edge of $\mathbf{I}$;

Step 4: Obtain an initial LCF thematic map (**LCFTM**);

Step 5: Check for each pixel in the same class between the initial **LCFTM** and $\mathbf{I}$; if not, produce **LCFTM** of the next iteration (Step 2 through Step 4 repeated) until each pixel with the same class between this **LCFTM** and that of the last iteration, or repeatedly exchanging the **LCFTM**s between this and the last iterations;

Step 6: Obtain the final **LCFTM**.

Homogeneity evaluation of resulting thematic map

To hypothesize that there would be a high correlation between classification accuracy and image homogeneity, in this research, a homogeneity index was introduced into the performance evaluation of heterogeneous class removal. Prior to homogeneity index calculation, a co-occurrence matrix must be calculated for resulting thematic map, where class index values instead of gray level values are recorded. Thus, a resulting thematic map can be given four co-occurrence matrices calculated by the kernel window in the directions of 0 (horizontal), 45 (↗ diagonal), 90 (vertical), and 135 (↖ diagonal) degrees. The calculation of the homogeneity index (*HOM*) is shown as follows [Haralick et al., 1973], and each co-occurrence matrix is given a homogeneity index. The values of *HOM* range

between 0 and 1. The higher the *HOM* value is, the more homogenous the resulting thematic map is. Finally, the four homogeneity indices are averaged to obtain a comprehensive homogeneity index [Yang et al., 2011]:

$$P_{ij} = \frac{M_{ij}}{\sum\limits_{i=1}^{n}\sum\limits_{j=1}^{n} M_{ij}} \quad [9]$$

$$HOM = \sum\limits_{i=1}^{n}\sum\limits_{j=1}^{n} \frac{P_{ij}}{1+(i-j)^2} \quad [10]$$

where P_{ij} denotes the probability in the $n{\times}n$ co-occurrence matrix M_{ij}.
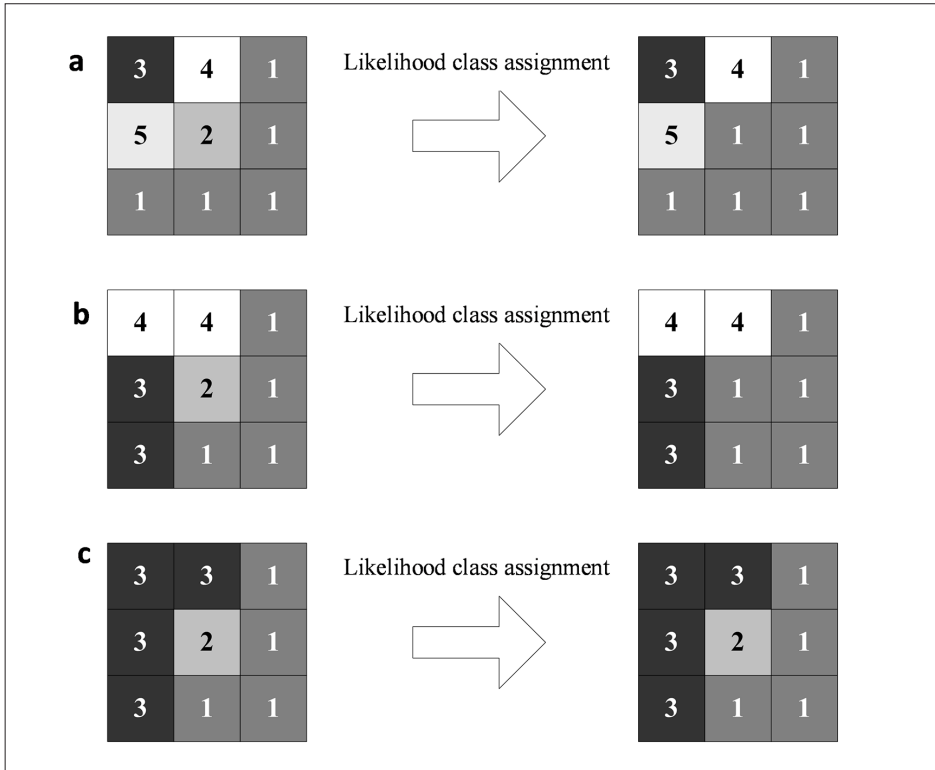

Figure 1 - Illustration of likelihood class assignments: (a) Class 1 is the only neighbourhood class that consists of 5 elements or more, thus is selected as the likelihood class 2. (b) Among the neighbourhood classes, Class 1 consists of the most elements, thus is selected as the likelihood class 2. (c) Class 2 is uncertain, as Classes 1 and 3 have the same number of elements.

Experimental materials

This research selected three hyperspectral remote sensing datasets, including two Airborne Visible/Infrared Imaging Spectrometer (AVIRIS) datasets and one Reflective Optics Spectrographic Imaging Instrument (ROSIS) dataset, from the website of Hyperspectral Remote Sensing Scenes (Available on-line at: http://www.ehu.es/ccwintco/index.php/ Hyperspectral_Remote_Sensing_Scenes) as the experimental materials. The experimental materials are introduced as follows.

1) Salinas-A scene: The Salinas image consisting of 512×217 pixels was produced by the 224-band AVIRIS sensor with high spatial resolution of 3.7 m, and a high spectral resolution of about 0.0094 μm (spectral reflection bands in the wavelength ranging 0.4 through 2.5 μm). The Salinas-A scene consisting of 83×86 pixels is a small sub scene of the Salinas image, located within the Salinas image at [rows, columns] = [158~240, 591~676]. In the Salinas-A scene image, the 20 water absorption bands, including bands 108 through 112, 154 through 167, and 224, were discarded so that the residual 204 bands were employed in this research. Figure 2 shows a false-colour image of the Salinas-A scene consisting of band 45 (red), band 25 (green), and band 15 (blue) and its corresponding ground data containing 6 classes. About a fourth or a third of one class was chosen as training samples (see Tab. 1). The larger the class, the higher the percentage of training samples.

2) Indian Pines test site: The Indian Pines test site was imaged as a hyperspectral remote sensing dataset of 145×145 pixels by the 224-band AVIRIS sensor. The original 224 bands were reduced to 200 bands by removing the water absorption bands, including bands 104 through 108, 150 through 163, and 220. Figure 3a shows the false-colour image of the Indian Pines test site consisting of band 45 (red), band 25 (green), and band 15 (blue), and its corresponding ground data is shown as Figure 3b. In Table 2, the percentages of training samples were arbitrarily determined in order to observe the influence of percentages of training samples on classification accuracy.

3) Pavia University scene: The ROSIS remote sensing dataset of the Pavia University scene consists of 610×340 pixels coupled with 103 spectral reflectance bands. The geometric resolution, spectral resolution, and wavelength range of the ROSIS sensor are 1.3 m, 0.004 μm, and 0.4 through 0.9 μm, respectively. Figure 4a shows the false-colour image of the Pavia University scene consisting of band 70 (red), band 50 (green), and band 30 (blue), and its corresponding ground data is shown as Figure 4b. In Table 3, about a seventh of one class was chosen as training samples.

Homogeneity evaluation for LCF post-classification

Classification results by LCF post-processing

Generally, eigenimages with an eigenvalue above 1 offer informative features for hyperspectral image classification [Teng, 2010]. However, a statistic based on the MNF analysis of this research indicates that the number of the eigenimages with an eigenvalue above 1 is extremely high. In this paper, an eigenvalue above 2 is recommended for the selection of eigenimages. The attributes of the selected MNF eigenimages for the hyperspectral image classification are shown in Table 4.
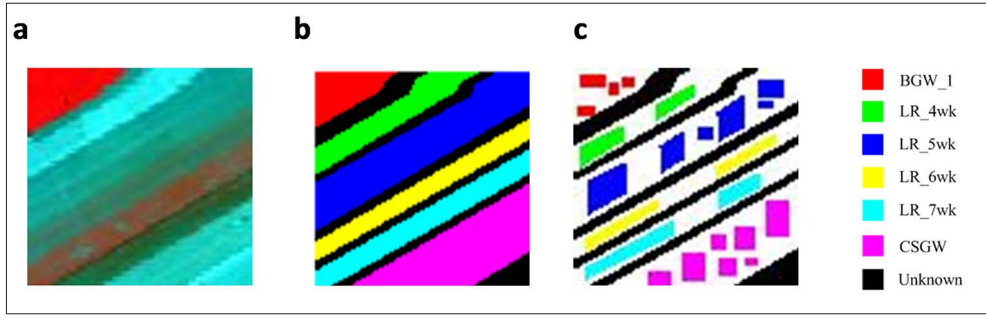
Figure 2 - AVIRIS dataset of Salinas-A scene: (a) False-colour image consists of band 45 (red), band 25 (green), and band 15 (blue). (b) Ground data contains 6 classes, including Brocoli_Green_ Weeds_1 (BGW_1), Lettuce_Romaine_4wk through Lettuce_Romaine_7wk (denoted LR_4wk through LR_7wk, respectively), and Corn_Senesced_Green_Weeds (CSGW). (c) Regions of training samples.
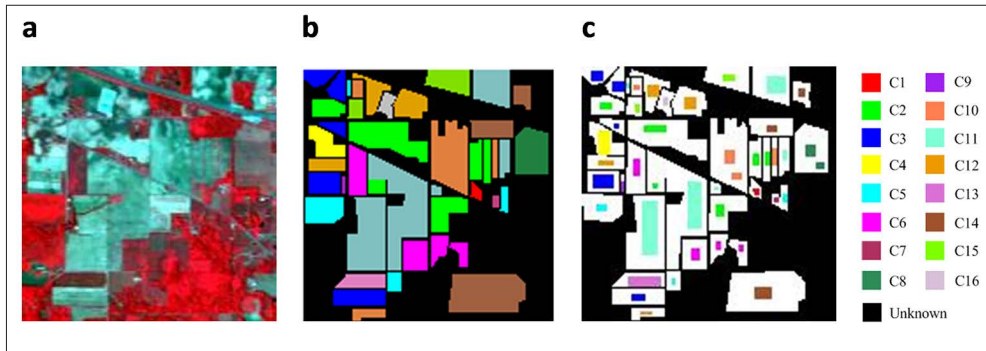

Figure 3 - AVIRIS data of Indian Pines test site: (a) False-colour image consists of band 45 (red), band 25 (green), and band 15 (blue). (b) Ground data contains 16 classes, including Alfalfa (C1), Corn-notill (C2), Corn-mintill (C3), Corn (C4), Grass-pasture (C5), Grass-trees (C6), Grass-pasture-mowed (C7), Hay-windrowed (C8), Oats (C9), Soybean-notill (C10), Soybean-mintill (C11), Soybean-clean (C12), Wheat (C13), Woods (C14), Buildings-Grass-Trees-Drives (C15), and Stone-Steel-Towers (C16). (c) Regions of training samples.

Table 1 - Sizes of classes and given training samples, and percentages of training samples in Salinas-A scene dataset.

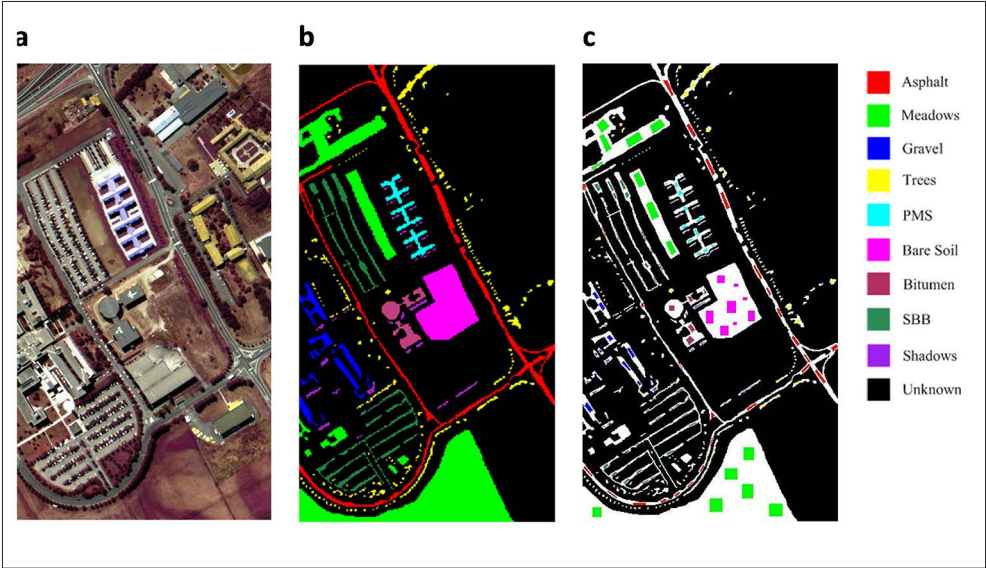| Class	Size of class (pixels)	Size of training samples (pixels)	Percentage (%)
BGW_1	391	100	6.00 (100/1667)
LR_4wk	616	189	11.34 (189/1667)
LR_5wk	1525	488	29.27 (488/1667)
LR_6wk	674	216	12.96 (216/1667)
LR_7wk	799	279	16.73 (279/1667)
CSGW	1343	395	23.70 (395/1667)
Total	5348	1667	100.00

Figure 4 - ROSIS data of Pavia University scene: (a) False-colour image consists of band 70(red), band 50 (green), and band 30 (blue). (b) Ground data contains 9 classes. PMS and SBB denote Painted Metal Sheets and Self-Blocking Bricks, respectively. (c) Regions of training samples.

Table 2 - Sizes of classes and given training samples, and percentages of training samples in Indian Pines test site dataset.

Class	Size of class (pixels)	Size of training samples (pixels)	Percentage (%)
C1	46	14	0.86 (14/1636)
C2	1428	143	8.74(143/1636)
C3	830	196	11.98(196/1636)
C4	237	84	5.13 (84/1636)
C5	483	39	2.38 (39/1636)
C6	730	76	4.65 (76/1636)
C7	28	6	0.37 (6/1636)
C8	478	51	3.12 (51/1636)
C9	20	6	0.37 (6/1636)
C10	972	105	6.42(105/1636)
C11	2455	556	33.98(556/1636)
C12	593	108	6.60(108/1636)
C13	205	108	6.60(108/1636)
C14	1265	98	5.99 (98/1636)
C15	386	36	2.20 (36/1636)
C16	93	10	0.61 (10/1636)
Total	10249	1636	100.00

Table 3 - Sizes of classes and given training samples, and percentages of training samples in Pavia University scene dataset.

Class	Size of class (pixels)	Size of training samples (pixels)	Percentage (%)
Asphalt	6631	976	15.59 (976/6259)
Meadows	18649	2713	43.35(2713/6259)
Gravel	2099	316	5.05 (316/6259)
Trees	3064	455	7.27 (455/6259)
PMS	1345	201	3.21 (201/6259)
Bare Soil	5029	748	11.95 (748/6259)
Bitumen	1330	194	3.10 (194/6259)
SBB	3682	515	8.23 (515/6259)
Shadows	947	141	2.25 (141/6259)
Total	42776	6259	100.00

Table 4 - Attributions of selected MNF eigenimages for hyperspectral image classification.

Hyperspectral remote sensing dataset	Bands of eigenimage dataset	Percentage of cumulated eigenvalues (%)
Salinas-A	1~14	54.48
Indian Pines test site	1~15	35.75
Pavia University	1~8	41.49

Depending upon the sites of training samples, as shown in Figures 2c, 3c and 4c, the multi-class SVM classification with Gaussian RBF kernel was performed to classify the hyperspectral remote sensing dataset based on the selected eigenimages. For the Gaussian RBF kernel, the penalty parameter C and the width r of x_i were suggested as 1024 and 2^{-7}, respectively [Tarabalka et al., 2010]. Figures 5 through 7 present the resulting thematic maps either with or without LCF post-processing for the Salinas-A scene, the Indian Pines test site, and the Pavia University scene, respectively. In the resulting thematic maps, not only the salt-and-pepper heterogeneous classes had been noticeably removed, but the original spatial structures of the classes were also not disturbed after LCF post-processing. The less the p elements in condition I are given, the better the effectiveness of LCF post-processing. Table 5 lists the accuracies of the resulting thematic maps and the efficiency estimation of LCF post-processing. If condition I coupled with less p elements is considered, not only a higher OA but also the computation of the LCF algorithm with more iterations are derived. For any hyperspectral remote sensing dataset, its optimal OA was derived by LCF post-processing based on condition II. Moreover, an exponential correlation ($R^2>0.9$) between image size and computation time was found in this research. Comparing the resulting thematic maps with and without LCF post-processing, the Salinas-A scene, the Indian Pines

test site, and the Pavia University scene were given the best OA improvements of 0.31%, 8.13% and 4.14%, respectively.

Table 6 lists the accuracies of the classes in the resulting thematic maps. For the Salinas-A scene, all 6 classes were given accuracies above 95%. Especially, the accuracies of BGW_1, LR_5wk and CSGW were 100%. Among the 6 classes, only LR_4wk had the significant accuracy improvement of 2.27% (from 96.27% to 98.54%), but none of the 6 classes had a decreased accuracy after LCF post-processing. For the Indian Pines test site, the 16 classes excluding C9 effectively improved their accuracies by LCF post-processing, which even offered C4, C8 and C13 accuracies of 100%. Also, LCF post-processing can result in the optimal accuracy for each class in the resulting thematic map of the Pavia University scene. Among the 9 classes, PMS had the best accuracy of 99.55% in the classification result without LCF post-processing, but LCF further raised the accuracy from 99.55% to 100%.

Homogeneity evaluation results

According to Equations [9] and [10], each map in Figures 5 through 7 calculated the homogeneity indices in four directions as well as the comprehensive homogeneity index (see Table7). Table7 shows that the homogeneities of the resulting thematic maps can be effectively improved by LCF post-processing. Also, LCF post-processing based on condition II led to the optimal homogeneity. The comprehensive homogeneity indices (the averaged values) of the resulting thematic maps of the Salinas-A scene, the Indian Pines test site, and the Pavia University scene were between 0.96 and 0.97, between 0.72 and 0.89, and between 0.76 and 0.90, respectively. Thus, the improved percentages of the comprehensive homogeneity indices were 1.04%, 23.61%, and 18.42% for the resulting thematic maps of the Salinas-A scene, the Indian Pines test site, and the Pavia University scene, respectively. This paper demonstrates that the higher the classification accuracy obtained by LCF post-processing, the higher the image homogeneity. The R^2 (square of Pearson coefficient) values between accuracy and comprehensive homogeneity index of the Salinas-A scene, the Indian Pines test site and the Pavia University scene are 0.9593, 0.9605 and 0.9071, respectively. This result demonstrates that there is a robust correlation between classification accuracy and image homogeneity. Via the obtained regression models, image homogeneity can be confidently predicted once classification accuracy is obtained.

Discussion

After LCF post-processing, OAs of 92.41% and 92.35% were obtained for the resulting thematic maps of the Indian Pines test site and the Pavia University scene, respectively. This result demonstrates that in addition to spatial-contextual or object-based image classifications [Chen, 2008; Liu et al., 2008], post classification filtering is also useful in improving the performance of pixel-wise image classification. In this section, the issues, including the influence of percentages of training samples on classification accuracy, and LCF post-processing vs. accuracy improvement, are discussed. Finally, some interesting points in this research are also revealed.
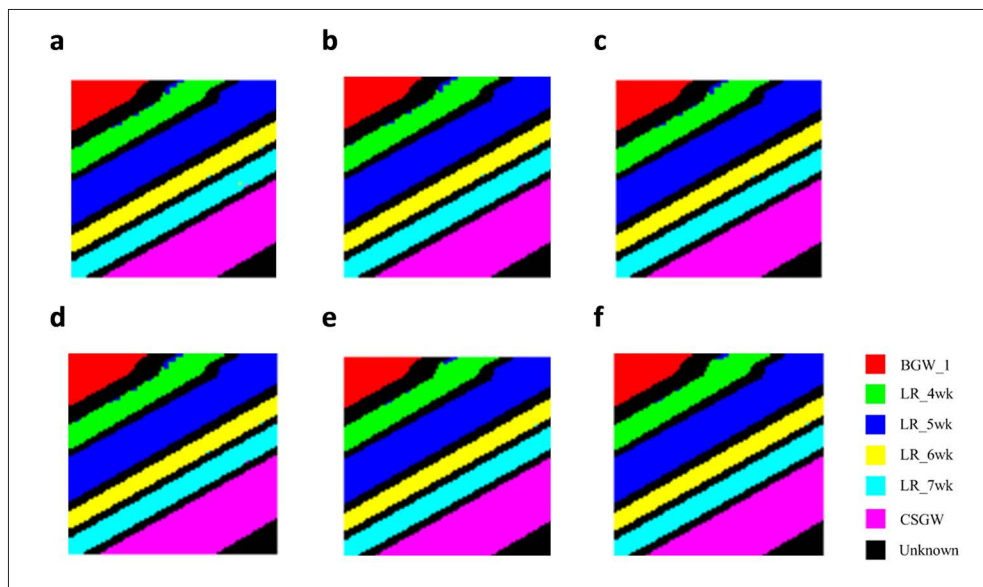
Figure 5 - Resulting thematic maps of Salinas-A scene: (a) Without LCF post-processing. (b) through (e) LCF post-processing based on condition I coupled with *p*=8, 7, 6 and 5, respectively. (f) LCF post-processing based on condition II.

Figure 6 - Resulting thematic maps of Indian Pines test site: (a) Without LCF post-processing. (b) through (e) LCF post-processing based on condition I coupled with *p*=8, 7, 6 and 5, respectively. (f) LCF post-processing based on condition II.

Figure 7 - Resulting thematic maps of Pavia University scene: (a) Without LCF post-processing. (b) through (e) LCF post-processing based on condition I coupled with *p*=8, 7, 6 and 5, respectively. (f) LCF post-processing based on condition II.
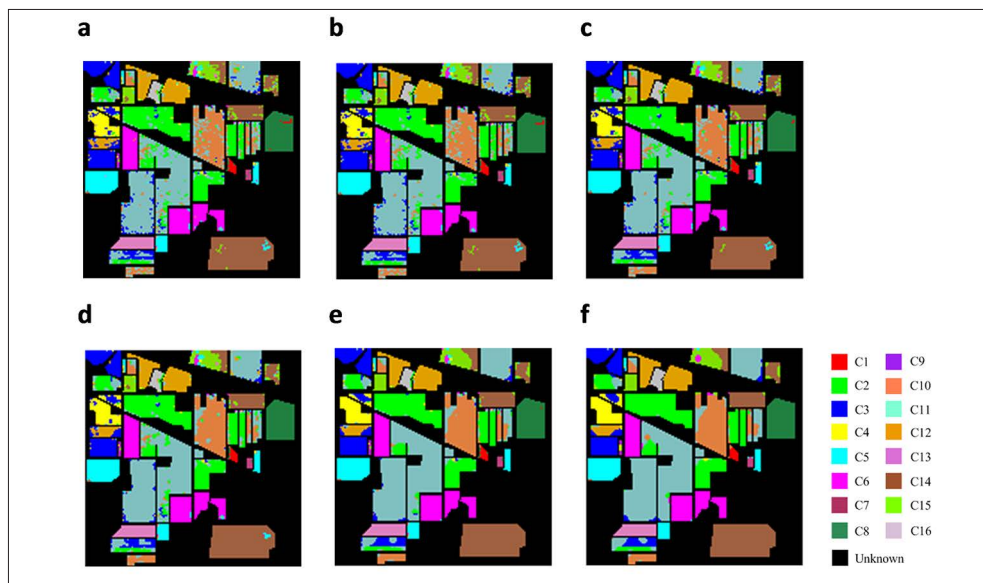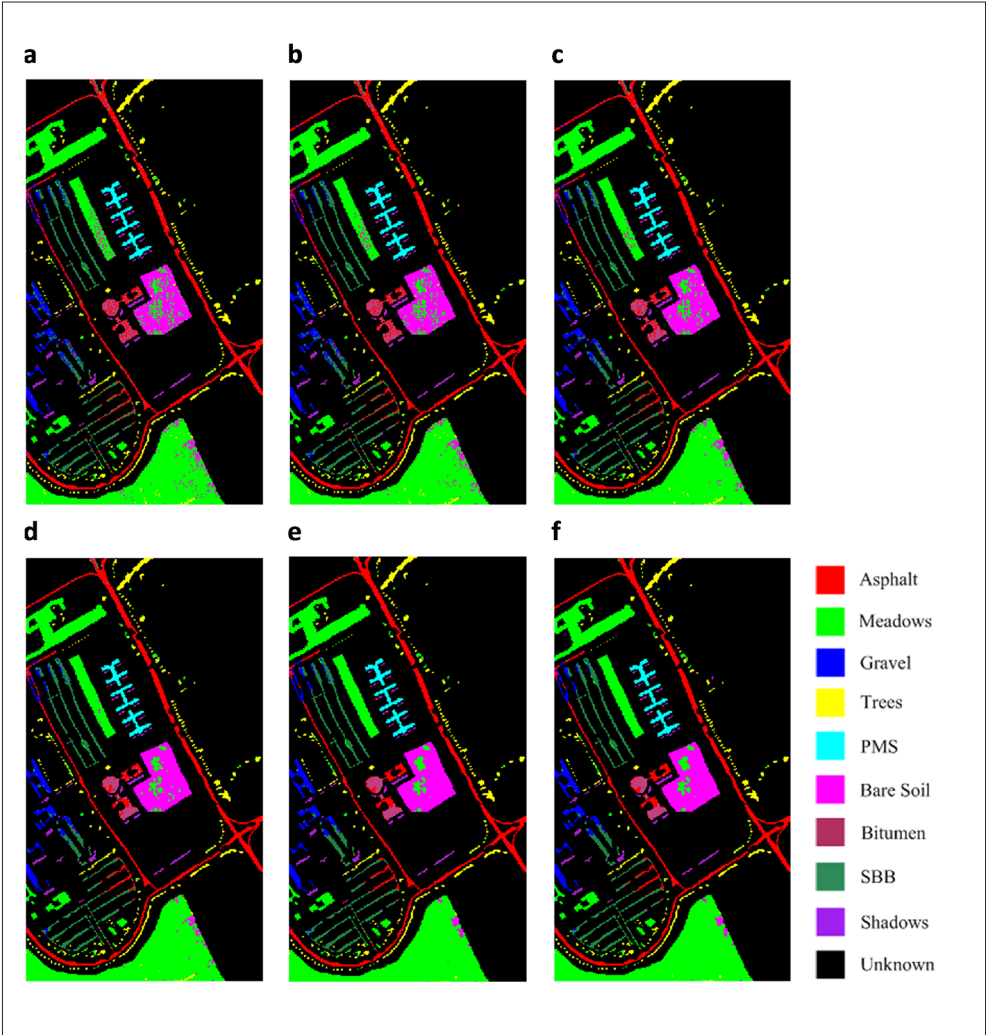
Table 5 - Accuracy estimation for resulting thematic maps with and without LCF post-processing.

Item	Hyperspectral remote sensing dataset	Without LCF post-processing	LCF post-processing				Condition II
			Condition I				
			p=8	*p*=7	*p*=6	*p*=5	
OA ± uncertainty [a] (%)	Salinas-A	99.50±0.28	99.51±0.28	99.51±0.28	99.53±0.28	99.78±0.19	99.81±0.18
	Indian Pines test site	84.28±1.62	84.69±1.60	86.04±1.54	87.90±1.45	91.47±1.24	92.41±1.18
	Pavia University	88.21±0.74	89.04±0.72	90.42±0.68	91.69±0.63	92.27±0.61	92.35±0.61
KHAT statistic	Salinas-A	0.994	0.994	0.994	0.994	0.997	0.998
	Indian Pines test site	0.820	0.825	0.840	0.862	0.902	0.913
	Pavia University	0.843	0.854	0.872	0.889	0.896	0.897
No. of iterations of the LCF algorithm	Salinas-A		1	1	4	6	10
	Indian Pines test site	-	1	5	7	41	14
	Pavia University		1	8	15	31	25
Computation time [b] (s)	Salinas-A		0.84	0.84	0.97	1.05	1.79
	Indian Pines test site	-	33.81	34.98	34.57	40.96	38.64
	Pavia University		2183.78	2205.93	2221.44	2243.71	2236.36

[a]95% confidence interval on *OA* (%).
[b]The LCF algorithm was run on a 2.5GHz PC with four CPUs.

Table 6 - Accuracies (%) of classes in resulting thematic maps.

Hyperspectral remote sensing dataset	Class	Without LCF post-processing	LCF post-processing				Condition II
			Condition I				
			p=8	*p*=7	*p*=6	*p*=5	
Salinas-A	BGW_1	100.00	100.00	100.00	100.00	100.00	100.00
	LR_4wk	96.27	96.27	96.27	96.43	98.21	98.54
	LR_5wk	100.00	100.00	100.00	100.00	100.00	100.00
	LR_6wk	99.70	99.70	99.70	99.70	99.85	99.85
	LR_7wk	99.75	99.87	99.87	99.87	100.00	100.00
	CSGW	100.00	100.00	100.00	100.00	100.00	100.00
Indian Pines test site	C1	80.43	80.43	80.43	82.61	80.43	89.13
	C2	82.63	83.12	84.03	86.06	89.08	92.23
	C3	73.61	73.49	73.86	73.73	76.27	75.18
	C4	82.70	82.70	86.08	89.87	97.89	100.00
	C5	95.45	95.86	95.86	96.27	97.31	98.76
	C6	97.40	97.81	98.08	98.49	99.86	99.86
	C7	89.29	89.29	92.86	92.86	92.86	92.86
	C8	97.91	98.33	99.37	100.00	99.79	100.00
	C9	75.00	75.00	75.00	75.00	75.00	60.00
	C10	72.43	72.94	76.44	81.79	86.63	85.80
	C11	83.14	84.07	85.70	88.31	94.75	95.44
	C12	85.83	85.83	87.86	88.36	90.39	91.74
	C13	99.51	99.51	99.51	99.51	99.51	100.00
	C14	91.70	91.86	92.96	94.78	96.52	97.47
	C15	61.66	61.40	62.95	64.25	70.98	72.54
	C16	83.87	83.87	83.87	81.72	87.10	97.85
Pavia University	Asphalt	91.92	93.08	94.72	96.28	96.55	96.80
	Meadows	94.62	95.39	96.49	97.70	98.61	98.69
	Gravel	68.03	68.94	71.08	72.37	72.84	72.84
	Trees	87.01	87.04	87.40	87.50	86.13	85.70
	PMS	99.55	99.63	99.63	99.70	99.78	100.00
	Bare Soil	79.82	81.43	83.89	87.35	89.28	89.32
	Bitumen	55.26	55.56	58.87	58.50	55.04	55.11
	SBB	77.95	78.76	80.15	80.58	81.67	81.86
	Shadows	99.16	99.16	99.16	99.26	99.05	99.37

Table 7 - Homogeneity indices of resulting thematic maps.

Map	HOM_0°	HOM_45°	HOM_90°	HOM_135°	Avg.
Fig. 5a	0.9737	0.9670	0.9640	0.9428	0.9619
Fig. 5b	0.9739	0.9672	0.9641	0.9429	0.9620
Fig. 5c	0.9740	0.9673	0.9641	0.9430	0.9621
Fig. 5d	0.9752	0.9686	0.9645	0.9436	0.9630
Fig. 5e	0.9777	0.9827	0.9657	0.9468	0.9682
Fig. 5f	0.9810	0.9861	0.9685	0.9507	0.9716
Fig. 6a	0.7742	0.6846	0.7285	0.6900	0.7193
Fig. 6b	0.7814	0.6918	0.7357	0.6972	0.7265
Fig. 6c	0.7970	0.7130	0.7589	0.7195	0.7471
Fig. 6d	0.8223	0.7449	0.7924	0.7512	0.7777
Fig. 6e	0.8680	0.8067	0.8488	0.8144	0.8345
Fig. 6f	0.9164	0.8733	0.9060	0.8788	0.8936
Fig. 7a	0.7718	0.7465	0.7737	0.7366	0.7571
Fig. 7b	0.7855	0.7602	0.7874	0.7503	0.7709
Fig. 7c	0.8121	0.7846	0.8124	0.7749	0.7960
Fig. 7d	0.8506	0.8195	0.8492	0.8107	0.8325
Fig. 7e	0.8918	0.8703	0.8904	0.8604	0.8782
Fig. 7f	0.9106	0.8903	0.9099	0.8832	0.8985

Influence of percentages of training samples on classification accuracy

Theoretically, a class is expected to have high classification accuracy if the percentage of its given training samples is relatively large in the entire training sample set. However, in the Salinas-A scene dataset BGW_1 depending upon a training sample set of 6%, a classification accuracy of 100% was obtained, which equals the accuracies of LR_5wk and CSGW depending upon training sample sets of 29.27% and 23.70%, respectively. In Table 2, C7 and C9, due to their small spatial structures, both had the smallest percentage of training samples. Although the lowest classification accuracy of 75% was offered for C9, the classification accuracy of 89.29% of C7 is superior to those of many other classes. In addition, Table 3 shows that Meadows occupies almost half of the Pavia University scene dataset. Nevertheless, of the 9 classes, Meadows did not obtain the best classification accuracy.

The linear correlations (R^2) between classification accuracy and percentages of training samples in the Indian Pines test site and Pavia University scene datasets are 2.2×10^{-3} and 8.54×10^{-2}, respectively. This result demonstrates that the influence of percentages of training samples on classification accuracy is insignificant.

LCF post-processing vs. accuracy improvement

Table 8 illustrates the accuracy improvements of the Salinas-A scene, Indian Pines test site, and Pavia University scene datasets by LCF post-processing. In the Salinas-A scene dataset, with the exception of BGW_1, LR_5wk and CSGW, the other classes demonstrate

positive accuracy improvements. The less p elements introduced into condition I, the better the accuracy improvement derived. In spite of this, the best accuracy improvement in each class was obtained when condition II was introduced into LCF post-processing.

Giving less p elements for condition I does not necessarily result in LCF post-processing achieving a better accuracy improvement. For example, LCF post-processing based on condition II and condition I coupled with p=6 offers negative accuracy improvements for C9 and C16, respectively. Giving less p elements for condition I would result in a significant change of the resulting thematic maps before and after LCF post-processing. Unfortunately, a resulting thematic map with LCF post-processing is sometimes over processed, so as to deteriorate the accuracy improvement. Condition II compared with condition I will usually assist LCF post-processing in deriving the largest accuracy improvement. However, LCF post-processing based on condition II gave C9 a negative accuracy improvement of 15% due to the improper assignment of C4 for 3 pixels of C9. Among the 16 classes, C4 obtained the largest accuracy improvement of 17.30%, and C11, being the largest, obtained the most pixels, i.e. 302 (2455×12.30%) pixels, with class correction.

Table 8 also shows that LCF post-processing is useful in the accuracy improvement of the Pavia University scene dataset. Unfortunately, Trees and Bitumen obtain several negative accuracy improvements when LCF post-processing based on either condition I coupled with p=5 or condition II are adopted. Bitumen for example, suffers from the misclassification of Asphalt so that its accuracy in the resulting thematic map without LCF post-processing is only 55.26%. Although the heterogeneous Asphalt scattering over Bitumen had been mostly removed, Bitumen could still not obtain an effective accuracy improvement because the Asphalt scattering was simply massed rather than transformed into Bitumen. In addition, the heterogeneous Meadows scattering over Bare Soil in Figure 7a shows that most of the Meadows scattering was transformed into Bare Soil by LCF post-processing based on condition II. As a result, Bare Soil has good accuracy improvement of 9.50%.

Summary of research findings
In this research, some interesting points are revealed as follows:
- According to image size, the Salinas-A scene, the Indian Pines test site, and the Pavia University scene can be regarded as small, middle and large image datasets, respectively. The computation time required by the LCF algorithm is exponentially increased as larger remote sensing datasets are processed.
- LCF is robust and effective in the accuracy improvement of pixel-wise classification data. In other words, a more accurate thematic map can be produced by likelihood class assignment.
- A class with extremely small spatial structure, such as grass-pasture-mowed (C7) in the Indian Pines test site dataset, can be appropriately recognized despite its lower percentage of training samples.
- LCF post-processing results in better accuracy improvement based on condition II rather than condition I. This is because, compared to condition I, condition II effectively assists LCF post-processing in transforming a resulting thematic map into a better map.
- There is a high positive relationship between class homogeneity and classification accuracy. LCF post-processing is simultaneously helpful for improving class

homogeneity as well as classification accuracy.

- Heterogeneous classes with disk spatial structures of radius n pixels ($n{\geq}2$) cannot be effectively filtered in this research. In further work, a kernel with disk spatial structure with a radius of 3 or 4 pixels may be introduced into LCF to observe the heterogeneous class filtering performance.

Table 8 - Accuracy improvement (%) of resulting thematic maps of hyperspectral remote sensing datasets with against without LCF post-processing.

Hyperspectral remote sensing dataset	Class	Condition I				Condition II
		$p=8$	$p=7$	$p=6$	$p=5$	
Salinas-A	BGW_1	0.00	0.00	0.00	0.00	0.00
	LR_4wk	0.00	0.00	0.16	1.95	2.27
	LR_5wk	0.00	0.00	0.00	0.00	0.00
	LR_6wk	0.00	0.00	0.00	0.15	0.15
	LR_7wk	0.13	0.13	0.13	0.25	0.25
	CSGW	0.00	0.00	0.00	0.00	0.00
Indian Pines test site	C1	0.00	0.00	2.17	0.00	8.70
	C2	0.49	1.40	3.43	6.44	9.59
	C3	-0.12	0.24	0.12	2.65	1.57
	C4	0.00	3.38	7.17	15.19	17.30
	C5	0.41	0.41	0.83	1.86	3.31
	C6	0.41	0.68	1.10	2.47	2.47
	C7	0.00	3.57	3.57	3.57	3.57
	C8	0.42	1.46	2.09	1.88	2.09
	C9	0.00	0.00	0.00	0.00	-15.00
	C10	0.51	4.01	9.36	14.20	13.37
	C11	0.94	2.57	5.17	11.61	12.30
	C12	0.00	2.02	2.53	4.55	5.90
	C13	0.00	0.00	0.00	0.00	0.49
	C14	0.16	1.26	3.08	4.82	5.77
	C15	-0.26	1.30	2.59	9.33	10.88
	C16	0.00	0.00	-2.15	3.23	13.98
Pavia University	Asphalt	1.16	2.81	4.36	4.63	4.89
	Meadows	0.77	1.87	3.08	3.98	4.07
	Gravel	0.91	3.05	4.34	4.81	4.81
	Trees	0.03	0.39	0.49	-0.88	-1.31
	PMS	0.07	0.07	0.15	0.22	0.45
	Bare Soil	1.61	4.08	7.54	9.47	9.50
	Bitumen	0.30	3.61	3.23	-0.23	-0.15
	SBB	0.81	2.20	2.63	3.72	3.91
	Shadows	0.00	0.00	0.11	-0.11	0.21

Conclusions

In this study, the application of a likelihood class filter (LCF) to improve remote sensing data classification was proposed. Experiments were carried out on three hyperspectral remote sensing datasets, including the Salinas-A scene, the Indian Pines test site and the Pavia University scene, and different parameters involved with LCF were also tested. The experimental result demonstrates that LCF is robust in improving class homogeneity so as to achieve higher classification accuracy. LCF was demonstrated that it is useful in post classification filtering to remote sensing dataset with high spatial resolution, such as 1.3 m/pixel of the Pavia University scene, or moderate spatial resolution, such as 20 m/pixel of the Indian Pines test site.

The issue of hyperspectral image classification is still open to further study, and many novel spectral-spatial classification techniques are being presented [He and Li, 2015; Tan et al., 2015; Yang et al., 2015]. The developed spectral-spatial classification techniques use hyperspectral image pre-processing to achieve accuracy improvement, whereas this research developed LCF post-processing instead of the traditional pre-processing techniques to improve hyperspectral image classification. If a good result is obtained by the developed spectral-spatial classification techniques, this research ensures that LCF post-processing can further optimize the result. However, LCF still cannot effectively filter heterogeneous classes with disk spatial structures with a radius of n pixels ($n \geq 2$) so this accuracy improvement is limited. Further research will be devoted to reform the current LCF kernel, e.g. enlarging size of LCF kernel, to facilitate accuracy improvement of thematic maps with multiple land features. If the size of kernel is enlarged, more parameters p in condition I needed to be considered. Fortunately, our experimental result shows that condition II outperforms condition I. This result also means that condition II is useful to assist LCF algorithm in likelihood class assignment in spite of giving various sizes of kernels.

Acknowledgements

References

Akbari D., Safari A., Homayouni S. (2014) - *Object-based hyperspectral classification of urban areas by using marker-based hierarchical segmentation*. Photogrammetric Engineering and Remote Sensing, 80 (10): 963-970. doi: http://dx.doi.org/10.14358/PERS.80.10.963.

Chen C.H., Ho P.G.P. (2008) - *Statistical pattern recognition in remote sensing*. Pattern Recognition, 41 (9): 2731-2741. doi: http://dx.doi.org/10.1016/j.patcog.2008.04.013.

Chen D.M. (2008) - *A standardized probability comparison approach for evaluating and combining pixel-based classification procedures*. Photogrammetric Engineering and Remote Sensing, 74 (5): 601-609. doi: http://dx.doi.org/10.14358/PERS.74.5.601.

Du P., Tan K., Xing X. (2010) - *Wavelet SVM in reproducing kernel Hilbert space for hyperspectral remote sensing image classification*. Optics Communications, 283 (24):

4978-4984. doi: http://dx.doi.org/10.1016/j.optcom.2010.08.009.

Du P., Tan K., Xing X. (2012) - *A novel binary tree support vector machine for hyperspectral remote sensing image classification*. Optics Communications, 285 (13-14): 3054-3060. doi: http://dx.doi.org/10.1016/j.optcom.2012.02.092.

García-Gutiérrez J., Mateos-García D., Garcia M., Riquelme-Santos J.C. (2015) - *An evolutionary-weighted majority voting and support vector machines applied to contextual classification of LiDAR and imagery data fusion*. Neurocomputing, 163: 17-24. doi: http://dx.doi.org/10.1016/j.neucom.2014.08.086.

Gualtieri J.A., Chettri S.R., Cromp R.F., Johnson L.F. (1999) - *Support vector machine classifiers as applied to AVIRIS data*. Summaries of the Eighth JPL Airborne Earth Science Workshop, February 1999, Pasadena, CA, USA.

Haralick R.M., Shanmugam K., Dinsten I. (1973) - *Texture features for image classification*. IEEE Transactions on Systems, Man and Cybernetics, 3 (6): 610-621. Available online at: http://www.cis.rit.edu/~cnspci/references/dip/segmentation/haralick1973.pdf.

He Z., Li J. (2015) - *Multiple data-dependent kernel for classification of hyperspectral images*. Expert Systems with Applications, 42 (3): 1118-1135. doi: http://dx.doi.org/10.1016/j.eswa.2014.09.004.

Huang H., Huang Y. (2014) - *Improved discriminant sparsity neighbourhood preserving embedding for hyperspectral image classification*. Neurocomputing, 136: 224-234. doi: http://dx.doi.org/10.1016/j.neucom.2014.01.010.

Huang X., Zhang L. (2008) - *An adaptive mean-shift analysis approach for object extraction and classification from urban hyperspectral imagery*. IEEE Transactions on Geoscience and Remote Sensing, 46 (12): 4173-4185. doi: http://dx.doi.org/10.1109/TGRS.2008.2002577.

Kumar A.S., Keerthi V., Manjunath A.S., van der Werff H., van der Meer F. (2010) - *Hyperspectral image classification by a variable interval spectral average and spectral curve matching combined algorithm*. International Journal of Applied Earth Observation and Geoinformation, 12 (4): 261-269. doi: http://dx.doi.org/10.1016/j.jag.2010.03.004.

Licciardi G., Marpu P.R., Chanussot J., Benediktsson J.A. (2012) - *Linear versus nonlinear PCA for the classification of hyperspectral data based on the extended morphological profiles*. IEEE Geoscience and Remote Sensing Letters, 9 (3): 447-451. doi: http://dx.doi.org/10.1109/LGRS.2011.2172185.

Liu J., Pattey E., Nolin M.C. (2008) - *Object-based classification of high resolution SAR images for within field homogeneous zone delineation*. Photogrammetric Engineering and Remote Sensing, 74 (9): 1159-1168. doi: http://dx.doi.org/10.14358/PERS.74.9.1159.

Marpu P.R., Pedergnana M., Mura M.D., Benediktsson J.A., Bruzzone L. (2013) - *Automatic generation of standard deviation attribute profiles for spectral–spatial classification of remote sensing data*. IEEE Geoscience and Remote Sensing Letters, 10 (2): 293-297. doi: http://dx.doi.org/10.1109/LGRS.2012.2203784.

Mura M.D., Villa A., Benediktsson J.A., Chanussot J., Bruzzone L. (2011) - *Classification of hyperspectral images by using extended morphological attribute profiles and independent component analysis*. IEEE Geoscience and Remote Sensing Letters, 8 (3): 542-546. doi: http://dx.doi.org/10.1109/LGRS.2010.2091253.

Ouma Y.O., Tateishi R. (2008) - *Urban-trees extraction from Quickbird imagery using multiscale spectex-filtering and non-parametric classification*. ISPRS Journal of

Photogrammetry & Remote Sensing, 63: 333-351. doi: http://dx.doi.org/10.1016/j.isprsjprs.2007.10.006.

Plaza A., Benediktsson J.A., Boardman J.W., Brazile J., Bruzzone L., Camps-Valls G., Chanussot J., Fauvel M., Gamba P., Gualtieri A., Marconcini M., Tilton J.C., Trianni G. (2009) - *Recent advances in techniques for hyperspectral image processing*. Remote Sensing of Environment, 113 (Supplement 1): S110-S122. doi: http://dx.doi.org/10.1016/j.rse.2007.07.028.

Samadzadegan F., Hasani H., Schenk T. (2012) - *Determination of optimum classifier and feature subset in hyperspectral images based on ant colony system*. Photogrammetric Engineering and Remote Sensing, 78 (12): 1261-1273. doi: http://dx.doi.org/10.14358/PERS.78.11.1261.

Su H., Du P. (2014) - *Multiple classifier ensembles with band clustering for hyperspectral image classification*. European Journal of Remote Sensing, 47: 217-227. doi: http://dx.doi.org/10.5721/EuJRS20144714.

Sun W., Halevy A., Benedetto J.J., Czaja W., Liu C., Wu H., Shi B., Li W. (2014) - *UL-Isomap based nonlinear dimensionality reduction for hyperspectral imagery classification*. ISPRS Journal of Photogrammetry and Remote Sensing, 89: 25-36. doi: http://dx.doi.org/10.1016/j.isprsjprs.2013.12.003.

Tan K., Hu J., Li J., Du P. (2015) - *A novel semi-supervised hyperspectral image classification approach based on spatial neighborhood information and classifier combination*. ISPRS Journal of Photogrammetry and Remote Sensing, 105: 19-29. doi: http://dx.doi.org/10.1016/j.isprsjprs.2015.03.006.

Tarabalka Y., Chanussot J., Benediktsson J.A. (2010) - *Segmentation and classification of hyperspectral images using watershed transformation*. Pattern Recognition, 43 (7): 2367-2379. doi: http://dx.doi.org/10.1016/j.patcog.2010.01.016.

Teng S.B. (2010) - *ENVI (Image Analysis and Classification in Remote Sensing for ENVI)*. Science, Beijing, China.

Tu Z., van der Aa N., Gemeren C.V., Veltkamp R.C. (2014) - *A combined post-filtering method to improve accuracy of variational optical flow estimation*. Pattern Recognition, 47 (5): 1926-1940. doi: http://dx.doi.org/10.1016/j.patcog.2013.11.026.

Velasco-Forero S., Angulo J. (2013) - *Classification of hyperspectral images by tensor modeling and additive morphological decomposition*. Pattern Recognition, 46 (2): 566-577. doi: http://dx.doi.org/10.1016/j.patcog.2012.08.011.

Villa A., Chanussot J., Benediktsson J.A., Jutten C., Dambreville R. (2013) - *Unsupervised methods for the classification of hyperspectral images with low spatial resolution*. Pattern Recognition, 46 (6): 1556-1568. doi: http://dx.doi.org/10.1016/j.patcog.2012.10.030.

Yang L., Yang S., Li S., Zhang R., Liu F., Jiao L. (2015) - *Coupled compressed sensing inspired sparse spatial-spectral LSSVM for hyperspectral image classification*. Knowledge-Based Systems, 79: 80-89. doi: http://dx.doi.org/10.1016/j.knosys.2015.01.006.

Yang M.D. (2007) - *A genetic algorithm (GA) based automated classifier for remote sensing imagery*. Canadian Journal of Remote Sensing, 33 (3): 203-213. doi: http://dx.doi.org/10.5589/m07-020.

Yang M.D., Su T.C. (2008) - *Automated diagnosis of sewer pipe defects based on machine learning approaches*. Expert Systems with Applications, 35 (3): 1327-1337. doi: http://dx.doi.org/10.1016/j.eswa.2007.08.13.

Yang M.D., Su T.C., Pan N.F., Liu P. (2011) - *Feature extraction of sewer pipe defects using wavelet transform and co-occurrence matrix*. International Journal of Wavelets Multiresolution and Information Processing, 9 (2): 211-225. doi: http://dx.doi.org/10.1142/S0219691311004055.

Yang R., Gabbouj M., Neuvo Y. (1995) - *Fast algorithms for analyzing and designing weighted median filters*. Signal Processing, 41 (2): 135-152. doi: http://dx.doi.org/10.1016/0165-1684(94)00096-I.

Zhang L., Huang X. (2010) - *Object-oriented subspace analysis for airborne hyperspectral remote sensing imagery*. Neurocomputing, 73 (4-6): 927-936. doi: http://dx.doi.org/10.1016/j.neucom.2009.09.011.